

引用格式：特里莫诺娃·玛丽亚，斯特凡诺夫·尤里，杜宾亚·尼基塔，等，2025. 类岩材料力学特性非弹性变形模型构建综合研究[J]. 地质力学学报, 31(3): 475-490. DOI: 10.12090/j.issn.1006-6616.2024094

Citation: TRIMONOVA M, STEFANOV Y, DUBINYA N, et al., 2025. A comprehensive study of the mechanical properties of rock-like materials for inelastic deformation model establishment[J]. Journal of Geomechanics, 31(3): 475-490. DOI: 10.12090/j.issn.1006-6616.2024094

## 类岩材料力学特性非弹性变形模型构建综合研究

特里莫诺娃·玛丽亚<sup>1</sup>, 斯特凡诺夫·尤里<sup>2,3</sup>, 杜宾亚·尼基塔<sup>4,5</sup>, 巴克耶夫·鲁斯塔姆<sup>2,3</sup>

TRIMONOVA Mariia<sup>1</sup>, STEFANOV Yuri<sup>2,3</sup>, DUBINYA Nikita<sup>4,5</sup>, BAKEEV Rustam<sup>2,3</sup>

1. 俄罗斯科学院萨多夫斯基地球圈层动力学研究所, 莫斯科 俄罗斯 119334;
2. 俄罗斯科学院西伯利亚分院石油地质与地球物理研究所, 新西伯利亚 俄罗斯 630090;
3. 俄罗斯科学院西伯利亚分院强度物理与材料科学研究所, 托木斯克 俄罗斯 634055;
4. 莫斯科物理与技术学院应用地球物理中心, 多尔戈普鲁德内 俄罗斯 141701;
5. 俄罗斯科学院施密特地球物理研究所, 莫斯科 俄罗斯 123995

1. *Sadovsky Institute of Geosphere Dynamics, Russian Academy of Sciences, Moscow 119334, Russia;*
2. *Institute of Petroleum Geology and Geophysics, Siberian Branch of Russian Academy of Sciences, Novosibirsk 630090, Russia;*
3. *Institute of Strength Physics and Materials Science, Siberian Branch of Russian Academy of Sciences, Tomsk 634055, Russia;*
4. *Center of Applied Geophysics, Moscow Institute of Physics and Technology, Dolgoprudny 141701, Russia;*
5. *Schmidt Institute of Physics of the Earth, Russian Academy of Sciences, Moscow 123995, Russia*

### A comprehensive study of the mechanical properties of rock-like materials for inelastic deformation model establishment

**Abstract:** [Objective] The work is devoted to the study of irreversible deformation of artificial samples subjected to a set of standard experiments, with an aim to study their mechanical properties. The principal idea of the study is related to the preparation of an artificial material with an established constitutive behavior model. The existence of such a well-described material provides future opportunities to conduct controllable experiments on various mechanical processes in rock-like material for further development and validation of theoretical models used in rock mechanics. [Methods] A set of artificial samples was prepared for careful assessment through a number of loading tests. Experimental work was carried out to determine the rheological properties under conditions of triaxial compression tests and uniaxial tension. Triaxial loading tests are completed for 9 samples with varying radial stress levels (0–5 MPa). The samples are loaded up to the yield point with control of radial and volumetric strain. The experimental results, which contain the obtained interrelationships between axial and radial stresses and strains, are analyzed using the Drucker-Prager yield surface. Material hardening is taken into account through the non-associated plastic flow law with the cap model. Numerical modeling of sample loading is performed through the finite difference method. Mathematical model parameters are adjusted to minimize the discrepancy between numerical modeling results and experimental data. The design of a series of experimental studies necessary to determine all the parameters of the model has been studied. [Results] It is shown that the formulated mathematical model allows to reliably reproduce the inelastic behavior of the studied material, and it can be used to solve a set of applied problems in continuum mechanics, the problem of numerical simulation of hydraulic fracture growth in an

基金项目：俄罗斯联邦教育科学部的国家项目（125012100531-7）；基础科学研究（FWZZ-2022-0021）

This research is financially supported by the State assignment of the Ministry of Education and Science of the Russian Federation (Grant No. 125012100531-7) and the FNI Project (Grant No. FWZZ-2022-0021).

第一作者：特里莫诺娃·玛丽亚（1991—），女，在读硕士，岩石力学专业。Email: [trimonova.ma@gmail.com](mailto:trimonova.ma@gmail.com)

通信作者：斯特凡诺夫·尤里（1991—），男，博士，岩石力学专业。Email: [dubinya.nv@gmail.com](mailto:dubinya.nv@gmail.com)

收稿日期：2024-09-04；修回日期：2025-04-18；录用日期：2025-04-27；网络出版日期：2025-05-14；责任编辑：王婧

elastoplastic medium in particular. It was found that for the entire range of applied lateral loads (0 – 5 MPa), the elastic limit varied from 2 to 4 MPa, after which the material began to behave plastically. It was also determined that at lateral loads  $\geq 3$  MPa, compaction began to appear in the material beyond the yield point. Judging by the dependence of volumetric strains under a lateral load equal to 1.4 MPa, compaction should begin to appear even at lateral loads lower than 3 MPa. [Conclusion] Taking the plastic behavior of the material into account is necessary when moving on to modeling the hydraulic fracturing process in such a material, and the resultant plasticity parameters for the model material can be used for numerical modeling of elastoplastic deformation of the rock under consideration, including processes such as hydraulic fracture growth in a poroelastoplastic medium. [Significance] The suggested procedure to interpret results of experimental studies can be used for further numerical modeling of mechanical processes in rock masses with inelastic strain accumulation. This opportunity can increase the reliability of geomechanical models used for the optimization of hydrocarbon fields development.

**Keywords:** plastic deformation; internal friction; shear strength; triaxial compression; “Brazilian” test; loading diagrams

**摘要:** 文章旨在通过一系列标准化试验研究人造材料样品的不可逆变形行为, 探究其力学特性。研究的主要思路在于制备具有既定本构行为模型的人造材料样品。借助该材料特性明确的优势, 未来有望利用其对类岩石材料开展各类机械过程的可控试验, 为岩石力学领域理论模型的进一步发展及验证提供有力支撑。研究制备了1组人工样品, 对其进行加载试验和细致评估, 以确定三轴压缩试验和单轴拉伸条件下样品的流变特性。对其中9个样品进行了不同径向应力水平(0~5 MPa)的三轴加载试验, 在控制径向应变和体积应变的情况下, 将样品加载至屈服点。基于Drucker-Prager屈服面理论, 系统分析了轴向-径向应力应变关系实验数据, 并采用非关联塑性流动规律和盖帽模型考虑材料硬化效应。利用有限差分法对样品加载进行数值建模, 为确定模型参数设置了一系列试验, 通过调整数学模型参数, 尽量减少模拟结果与试验数据之间的差异。试验结果显示, 所建数学模型能够可靠复现所研究材料的非弹性行为, 并可用于解决连续介质力学中的各类实际问题, 特别是弹塑性介质中水力裂缝扩展的数值模拟。研究结果表明, 在0~5 MPa的侧向荷载作用下, 材料弹性极限为2~4 MPa, 超出此范围即进入塑性变形阶段; 当侧向荷载 $\geq 3$  MPa时, 材料在屈服点后会呈现压密现象。从1.4 MPa侧向荷载作用的体积应变变化规律可以推断, 材料在3 MPa以下的侧向荷载作用下即应开始产生压密效应。因此, 在对此类材料的水力压裂过程进行建模时, 必须考虑其塑性行为特征。由此得出的模型材料塑性参数可用于模拟研究岩体的弹塑性变形, 包括多孔弹塑性介质中的水力裂缝扩展等过程。文章提出的试验数据解释方法, 可用于开展岩体非弹性应变累积过程的数值模拟研究。该技术途径将有效提升油气田开发优化中所用地质力学模型的可靠性。

**关键词:** 塑性变形; 内摩擦力; 抗剪强度; 三轴压缩; 巴西劈裂试验; 加载图

中图分类号: TD315 文献标识码: A 文章编号: 1006-6616(2025)03-0475-16

DOI: 10.12090/j.issn.1006-6616.2024094

## 0 Introduction

The mechanical behavior of rocks is governed by their properties, the stress-strain state and external factors that cause changes to this state. Solving many applied problems requires modeling that can predict how geological media will behave under variable external loads.

When considering hydrocarbon deposits, we can note an increase in the number of unconventional reservoirs. The reservoir properties are determined by systems of tensile and shear fractures, which result from irreversible

strain localization(Schwab et al., 2017). When developing such reservoirs, the activation of natural fractures is observed when pressure fields in the environment change(Jin et al., 2023) or during operations to intensify the flow, for example, during hydraulic fracturing (Wang et al., 2023). Classical poroelastic models do not always allow adequate modeling of the mechanical behavior of rock masses during development (Weng et al., 2013). This is confirmed by the results of laboratory and field studies(Fu et al., 2022), highlighting the need to develop methods of modeling mechanical behavior of rocks, and to verify the results using

independent methods.

It is necessary to describe the behavior of the medium under load to solve problems of rock deformation. Geological media (soils and rocks) are media with a pronounced heterogeneous structure. Their behavior depends on stress state (Yang et al., 2012) and history of changes (Sathar et al., 2012). Elastic (Sun et al., 2017) and strength properties (Chen et al., 2023) depend on the internal structure of rocks. Depending on the loading conditions, as well as the structure of the material, deformation beyond the elasticity limit can vary and is accompanied by softening and hardening (Bésuelle et al., 2000; Sun et al., 2017; He et al., 2019). At low pressure, rocks are usually brittle, that is, grains and bonds between them are easily destroyed during inelastic deformation. With increasing pressure, they often behave like elastoplastic bodies and are destroyed in a viscous manner, with an accumulation of irreversible strain (Wong and Baud, 2012). Nowadays, various studies are devoted to the establishment of theoretical models capable of adequately describing inelastic deformation. There are several key directions in current published findings: brittle-ductile transition, describing the nature of post-failure processes of rock samples (Liu et al., 2023); micromechanical aspects of failure processes with special attention to changes in the inner structure of the rock due to inelastic strain accumulation (Sun et al., 2020; Tang et al., 2024; Wang et al., 2024). Certain studies consider inelastic strain accumulation in terms of damage accumulation with gradual reduction of current elasticity moduli: anisotropic models are currently being developed (Lyakhovskiy et al., 2022). Numerical simulations of the mentioned processes are currently performed with varying theoretical models and numerical procedures: some are dedicated to dilatancy and corresponding changes of the internal rock structure (Rong et al., 2013; Tan et al., 2015), some are more focused on compaction and seismic waves propagation (Omlin et al., 2018; Yarushina et al., 2020) with particular interest to strain rate dependent models (Cassiani et al., 2017). Apart from solving typical geomechanical reservoir problems (wellbore stability, hydraulic fracture design, etc.), the construction of a

constitutive model is also applied for the characterization of rock masses using seismic data: a recent study (Yang et al., 2024) proposed a method to evaluate rock porosity – a crucial factor for hydrocarbon reservoir development – based on triaxial loading tests results. At the same time, it is reported that a proper choice of the inelastic plastic flow law considerably effects the solutions of geomechanical reservoir problems (Amour et al., 2023), proving the importance of constructing and validating such models.

While compaction and dilation of rock samples in triaxial loading tests are often taken into account within theoretical models, both factors are considered in the models simultaneously. Seldom models (Hajjabadi and Nick, 2020) have been constructed for both dilatancy and compaction with a number of limitations related to the nature of rock stress state and properties (Zhang et al., 2024). While certain studies were proposed as a basis to use such constitutive models for crack propagation in fractured sandstones (Jiao et al., 2024) and coals (Ma et al., 2024), hydraulic fracturing design still requires a proper formulation of theoretical models and their validation using experimental data.

Hydraulic fracturing is one of the main methods for oil recovery enhancement. With the increasing development of unconventional reservoirs, characterized not only by low permeability, but also by inelastic behavior, there is a growing need to study hydraulic fracturing in such fields. At the same time, the fragility and plasticity of the rock have significant impact on the growth of hydraulic fractures, which must be taken into account when modeling (Van Dam et al., 2002). Basically, behavior beyond the elasticity limit is considered only in the vicinity of the fracture tip (Garagash, 2019). The associated plastic flow law is often used when describing such processes. But the application of the associated flow law does not provide quantitative agreement with the observed data, since the value of volumetric plastic deformation turns out to be greatly overestimated due to the fact that the dilatancy and internal friction coefficients remain interconnected (Vermeer and De Borst, 1984; Nikolaevskii, 1971). In addition, the description of the process of irreversible deformation accumulation requires taking hardening and softening into account.

It is necessary to conduct laboratory experiments of triaxial or true triaxial loading and analyze deformation diagrams of the rock in detail to determine the parameters of such models. The functionality of the formulated mathematical model can be confirmed only by means of numerical simulation with a comparison of the results obtained with experimental data.

This paper discusses the results of a series of experiments on triaxial loading of cylindrical samples using the technical facilities of the collective use center of the Institute of Earth Physics of the Russian Academy of Sciences (Veselovskiy et al., 2022). Previously, work on establishing the parameters of the elastic-plastic behavior model was carried out for certain classes of rocks (Stefanov et al., 2011; Garagash et al., 2018).

The results of studies on the mechanical properties of artificial materials were used to determine the parameters of the mathematical deformation model necessary to perform numerical modeling. The modeling results are used to discuss the design of a series of experiments required for the proper construction of mathematical models for the inelastic deformation of rock-like materials.

## 1 Experimental data

The selection and adaptation of the mathematical model, as well as the determination of its parameters, are based on experimental data on the behavior of the medium under external loading. A series of experiments was carried out to study the mechanical behavior of samples made of artificial material, which is a mixture of gypsum and cement at a ratio of 9:1. The use of an artificial material is due to the need of conducting series of experiments with samples of the same properties. It is a well-known problem in the field of reservoir geomechanics that the mechanical properties of rocks are very volatile, and it is almost impossible to find a pair of real samples with similar properties that affect fracture growth, primarily, defects in the inner structure of the rock. In turn, the preparation of artificial samples makes it possible to obtain material with properties of slight variability, providing that experimental results are of high reproducibility. The choice of gypsum and cement and the

particular ratio was based on the criteria of similarity theory. The detailed explanations of the ratio choice were given in a separate paper (Trimonova et al., 2017). Mixture composition was selected based on the need to replicate the growth of a radial crack propagating in a homogeneous rock mass at field conditions through a controllable test at laboratory conditions. Given the size of the experimental setup for physical modeling of hydraulic fracture growth, the mechanical parameters of the real rocks from hydrocarbon reservoirs located in Western Siberia, and the parameters of gypsum and cement in use, application of the set of dimensionless parameters (De Pater et al., 1994) made it possible to determine the optimal mixture properties used for the study.

To comprehensively study the properties of the material, two types of studies were performed: triaxial compression of cylindrical samples and determination of uniaxial tensile strength using the “Brazilian” test method. These detailed studies of the material made it possible to establish constitutive relationships and set up and verify a mathematical model that can be used to simulate the mechanical behavior of the material.

As part of the first series of experimental studies, cylindrical samples with diameters of 60 mm and heights of 120 mm were examined. According to triaxial loading testing standards, cylindrical specimens with a height-to-diameter ratio of 2:1 are preferable for rock mechanics problems (Omar and Sadrekarimi, 2015). The laboratory equipment used for the current study provides quality measurements for specimens with diameters between 30 mm and 100 mm (Veselovskiy et al., 2022) and corresponding heights. In addition, the chosen sample diameter of 60 mm makes it possible to obtain a sufficient number of samples from a single series of multiple tests to increase the accuracy of the experimental results.

The study of scale effects is beyond the scope of this paper. To examine the physical mechanisms of fracture is a separate topic that requires special studies using nonlocal mathematical models. The results of corresponding studies on similar materials (Williams et al., 2020) make it possible to assume that the obtained model parameters can be used to describe the mechanical behavior of the artificial material.

An elastoplastic model with a Drucker-Prager yield surface was chosen to interpret the experimental results. To carry out calculations for numerical modeling of deformation processes using the specified model, along with the dimensions of the sample and its density, it is necessary to know the following parameters: volumetric compression and shear moduli, initial cohesion, hardening coefficient, internal friction coefficient, dilatancy coefficient, and magnitude of shear plastic deformation at the peak strength. These parameters were determined using standard triaxial tests.

Experimental work to study the properties of the samples was carried out using the GCTS RTR4500 servohydraulic testing facility, belonging to a shared-use center of the Institute of Earth Physics of the Russian Academy of Sciences (Veselovskiy et al., 2022). This setup makes it possible to study samples under conditions of pseudo- and true triaxial compression. Conduction of the experiments involved the following steps:

0. Preparation of the samples. A typical procedure for the sample preparation has been completed before the experiments. Geometrical properties of the cylindrical samples were measured with high precision, the surfaces of the faces were polished and adjusted to maintain a parallelism error of the faces at a level not exceeding 0.02 mm. At the same time, the experimental equipment was calibrated using standard aluminum samples with known properties. The standard samples were subjected to triaxial loading, and measuring equipment was calibrated to maintain a relative discrepancy of less than 0.01% between the tabular elastic moduli in the elastic loading zone and the corresponding ratios of changes in measured stresses and strains (Lamé constants were chosen for calibration). The triaxial loading equipment and measurement system are described in detail in (Veselovskiy et al., 2022): a pair of linear variable differential transformers (LVDT) is used to control the quality of axial strain measurements: absolute difference between axial strain measurements should not exceed 0.001% for successful experiments (Yimsiri and Soga, 2002). Radial strain is measured using a local radial strain measurement system with an LVDT positioned at the center of the sample. Volumetric strain,

which is an important factor in subsequent analysis, is measured based on radial and axial strain, taking into account the effect of “barrel shape” for a parabolic profile of the deformed sample (Escribano et al., 2019). The described measurement system implies that a number of factors potentially leads to errors in strain measurements, including: seating, alignment, bedding errors, and compliance of the loading system. These problems are solved during the described calibration procedure for the equipment.

1. The sample, isolated from the penetration of external substances into it, is placed in the test chamber. After this, the chamber is filled with technical fluid.

2. The pressure of the fluid around the sample is increased to a certain specified value. Further, during the experiment, the fluid pressure is maintained at a constant level. This confining pressure uniformly applies a load to the side surface of the sample, corresponding to the radial stress  $\sigma_r$ .

Simultaneously with the increase in compressive pressure, an axial load equal to the fluid pressure is applied.

3. An additional axial load is applied at top and bottom of the sample according to the specified experimental program. Axial load was varied in a way to maintain the rate of change of axial deformation at a constant level ( $10^{-3} \text{ s}^{-1}$ ).

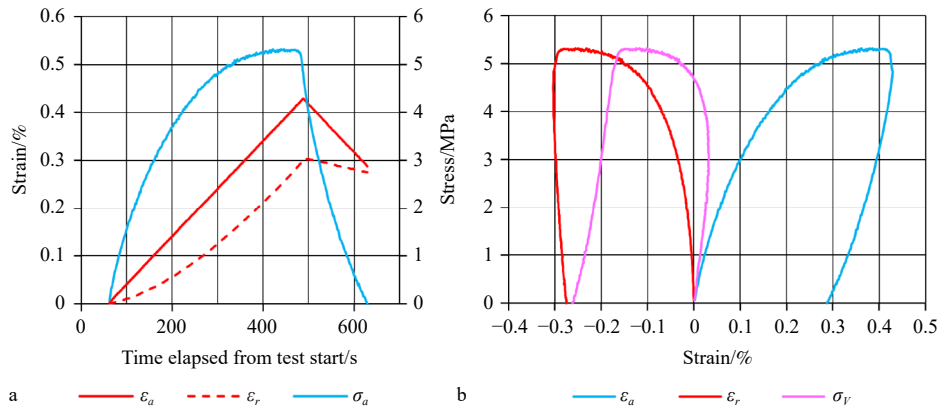
4. Loading is stopped and the sample is unloaded upon the completion of the loading program or when the sample is destroyed. When the stresses in the sample reach critical values, a failure occurs, resulting in a sharp decrease in stress while maintaining a constant rate of axial strain growth. After the stresses drop, at a moment determined by the technical operator, unloading of the sample begins: the axial load also decreases while maintaining a constant axial strain change rate.

5. After complete axial unloading, the fluid pressure around the sample is removed, the fluid leaves the chamber, and the destroyed sample is taken from the installation.

During the research, the values of the axial and radial strains of the sample are continuously recorded. Axial strain is defined as the relative change in the distance

between the support plates through which an axial load is transmitted to the sample.

Figure 1 shows typical load-time diagrams (Fig. 1a),



a—应力、应变与时间的关系; b—轴向应力与轴向、径向和体积应变的关系

图 1 典型试验结果

Fig. 1 Typical experimental results

(a) Dependence of stress and strain on time; (b) Dependence of axial stress on axial, radial, and volumetric strains

A series of experiments was carried out to study the effect of confining pressure on the properties of the material (Table 1). Table 1 shows the values of the

as well as stress-strain curves (Fig. 1b). The figure shows that the elasticity limit and strength for the samples under consideration were quite low.

maximum axial stress and volumetric strain achieved. In general, peak axial stress increases with radial stress.

表 1 试验约束条件

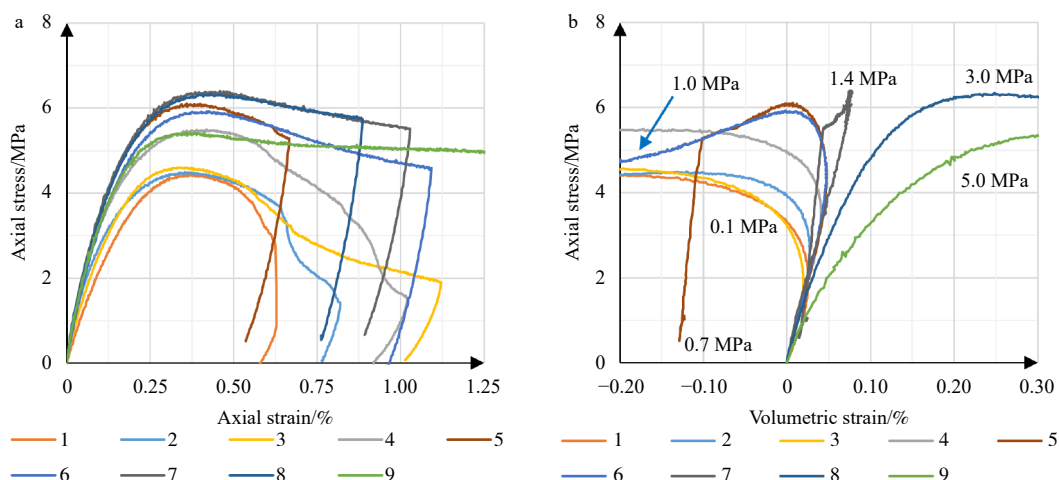
Table 1 Confining conditions in a series of experiments

Test set conditions	1	2	3	4	5	6	7	8	9
Radial stress/MPa	0.1	0.1	0.1	0.1	0.7	1.0	1.4	3.0	5.0
Peak axial stress/MPa	4.4	4.5	4.6	5.5	6.1	5.9	6.4	6.3	5.4
Volumetric strain after complete unloading/%	-1.0	-0.9	-2.2	-1.3	-0.1	-0.3	0.0	0.5	1.7

In experiments 1, 2, 3, 4, the lowest technically permissible radial stress was set. This makes it possible to study the behavior of a sample under conditions as close as possible to uniaxial compression. The obtained results are given in Fig. 2. Fig. 2a shows the obtained dependences of axial stress on axial deformation for all tests; Fig. 2b shows the dependence of the same parameter on volumetric strain. Fig. 2b also contains the level of radial stress maintained for each test in accordance with Table 1.

At the initial stages of loading, an increase in volumetric strain is observed, corresponding to elastic compression in all experiments. For the experiments 1, 2, 3, 4, it then begins to decrease significantly and enters the region of negative values (compressive strains are taken as

positive, and the tensile strains are taken as negative hereafter), i.e., the volume of the samples increases. After unloading the sample, the accumulated strain remains, i.e., it has a non-elastic (pseudo-plastic) nature. It has to be mentioned that while the elastic and pre-failure zones of the loading curves are similar in the four experiments with low radial stress, the behavior of the samples after achieving critical axial stress differs considerably. After its peak, the stress level decreases gradually, but at different rates for the samples subjected to identical loads. This results in variation in the accumulated inelastic strain observed after complete unloading ( $\sim 0.60\%$  for experiment 1,  $\sim 0.75\%$  for experiment 2, and  $1.00\%$  for experiment 3). Experiment 4 is not in line with the



a—轴向应力与轴向应变的关系; b—轴向应力与体积应变的关系

图 2 综合试验结果

Fig. 2 Combination of experimental results

(a) axial stress dependence on axial strain; (b) axial stress dependence on volumetric strain

previous tests as its peak stress level is significantly higher. We assume that these effects result from internal inhomogeneity of the prepared samples. Despite the careful sample preparation procedure, it is a complicated task to construct a homogeneous mixture with a lack of inner defects that have a high impact on strength. This series of experiments has been performed under the same conditions in order to evaluate discrepancies in loading curves associated with the sample preparation procedure. The observed level of discrepancy can be related to errors in the obtained data that must be accounted for in future analysis. The values of volumetric strain after unloading are given in Table 1 for each experiment. An increase in radial stress leads to a decrease in accumulated tensile strain. For the experiments with a maintained radial stress of 0.1 MPa, the accumulated strain is about 1%, but for the experiments 5, 6, and 7, where the radial stress is comparable to 1 MPa, the accumulated volumetric strain is reduced to fractions of a percent. The volumetric strain graphs for experiments at higher values of lateral compression have a fundamentally different form (experiments 8 and 9 with radial stresses of 3 and 5 MPa, respectively). The volumetric deformation curve deviates from the line of elasticity to the right. Volumetric deformations are positive throughout the loading process. This means that compaction is observed. Experiment 7, in which the radial stress was maintained at a level of 1.4

MPa, is closest to the boundary between two inelastic deformation modes (the volumetric strain accumulated by the sample after unloading turns out to be close to zero).

Thus, the completed series of experiments demonstrated two modes of plastic deformation in the samples, depending on the radial stress (Stefanov, 2023). At low values of radial stress (0.1 MPa), a dilatant deformation mode is realized, accompanied by an increase in the volume of the sample during plastic deformation. As the radial stress increases and exceeds 1.3 MPa, a compaction mode appears, accompanied by compression of the sample during the entire deformation period. The results of laboratory studies indicate that to fully describe the mechanical behavior of the material under load, a mathematical model is required that takes into account both deformation mechanisms.

## 2 Theoretical model

Assuming that strain rates consist of elastic and plastic parts, the stresses are determined by the ratio:

$$\dot{\sigma}_{ij} = \lambda (\dot{I} - \dot{I}^p) \delta_{ij} + 2\mu (\dot{\epsilon}_{ij} - \dot{\epsilon}_{ij}^p), \quad (1)$$

where:  $\sigma_{ij}$  are stress tensor components, the dot above means the time derivative;  $\lambda, \mu$  – Lamé parameters;  $I$  is the first invariant of the strain tensor deviator,  $\delta_{ij}$  is the Kronecker symbol. Note that in the given relationships, the rates of change of stresses and strains can be replaced by

their increments.

Taking into account the obtained data, the mathematical model should describe the deformation process in two modes: dilatancy and compaction. Accordingly, it should consist of two parts. For the first part, we will take the Drucker-Prager model as a base model (Drucker and Prager, 1952; Stefanov et al., 2011; Stefanov and Zharasbaeva, 2022; Stefanov, 2023), and write the plasticity criterion in the form:

$$f_1 = I_2 - \alpha I_1 - Y, \quad (2)$$

where  $I_2$  is the intensity of tangential stresses (the second invariant of the stress tensor),  $I_1$  is the pressure (the first invariant of the stress tensor),  $\alpha$  and  $Y$  are coefficients associated with the angle of internal friction and cohesion.

The increment of the inelastic or plastic part of the strain tensor, which is calculated when the stress state of the yield surface is reached, is determined by the flow equation:

$$d\varepsilon_{ij}^p = \lambda \frac{\partial g}{\partial \sigma_{ij}}, \quad (3)$$

where  $g(\sigma_{ij}, \varepsilon_{ij}^p)$  is the plastic potential, along the normal to which irreversible strain develops,  $\sigma_{ij}$  are the components of the stress tensor, and  $\varepsilon_{ij}^p$  are the components of the plastic deformation tensor. According to flow theory, plastic deformation develops along the normal to the plastic potential surface. It is written as follows:

$$g = I_2 - \beta I_1, \quad (4)$$

where  $\beta$  is the dilatancy coefficient, which determines the relationship between volumetric and shear strains.

During plastic deformation, the properties of the rock change. Therefore, hardening and subsequent degradation of the properties take place. In addition, the relationship between the shear and volumetric parts of the strain changes. Therefore, to describe the behavior of rocks beyond the elastic limit, it is necessary that the model parameters depend on the accumulated irreversible deformation. For this purpose, we will use the relations from (Drucker and Prager, 1952; Stefanov and Zharasbaeva, 2022; Stefanov, 2023). Equation for the cohesion that describes hardening and softening during

deformation is written as:  $Y = Y_0(1 + hA(\gamma^p) - D(\gamma^p))$ ,  $h$  – hardening coefficient,  $A(\gamma^p) = 2\gamma^p/\gamma^*$ ,  $D(\gamma^p) = (\gamma^p/\gamma^*)^2$ ,  $\gamma^p$  – intensity of shear plastic strain,  $e_{ij}^p = \varepsilon_{ij}^p - 1/3\varepsilon_{kk}^p\delta_{ij}$ ,  $\gamma^*$  – critical strain, after which degradation of the material predominates.

The first part of the yield surface, described by equation (2), corresponds to shear deformation, which is usually accompanied by dilatancy. According to experiments 8, 9 from Table 1, at radial loads exceeding 1.4 MPa, compaction is observed in the behavior of the samples. Therefore, the equation of the yield surface at pressures above the threshold value  $\sigma_0$ , at which compaction of the material begins, will take an elliptical form:

$$f_2 = \frac{(I_1 - \sigma_0)^2}{a^2} + \frac{I_2^2}{b^2} - 1 = 0, \text{ when } I_1 > \sigma_0, \quad (5)$$

where  $a = \sigma_1 - \sigma_0$ ,  $b = Y + \alpha\sigma_0$  are semi-axes of the ellipse.

During the compaction process, changes occur in the elliptical part of the yield surface. It can shift along the pressure axis and expand. In the model, this is described using the relation (Stefanov et al., 2011):  $\sigma_0(\varepsilon^p) = \sigma_0(\varepsilon^*/(\varepsilon^* + \varepsilon^p))^m$ , where  $\varepsilon^* = \phi^*$  is the initial porosity,  $\varepsilon^p$  is the volumetric deformation,  $m$  is a parameter.

An important point in describing the irreversible deformation of rocks is taking into account the dependence of the dilatancy coefficient on the stress state and the accumulated volumetric deformation. At a pressure below the threshold value  $\sigma_0$ , irreversible deformation develops in the dilatancy mode, and above it compaction. Accordingly, the dilatancy coefficient not only changes depending on the pressure, but also has a different sign in these regions. To describe this dependence, we use an expression (Stefanov et al., 2011), which ensures the necessary continuity and smoothness of the plastic potential function:

$$\beta(\sigma, \varepsilon^p) = \begin{cases} \beta_0 \left( \frac{\sigma_0 - I_1}{\sigma_0} \right)^n, & \text{when } I_1 \leq \sigma_0, \\ - \left( \frac{I_1 - \sigma_0}{\sigma_1 - \sigma_0} \right)^n, & \text{when } \sigma_0 < I_1 < \sigma_1. \end{cases} \quad (6)$$

A detailed description of the mathematical model used in the work is presented in (Stefanov et al., 2011).

Now the main task is to determine all the parameters

of the model for its use in calculations. Data from experiments performed on triaxial loading were analyzed to do that.

### 3 Analysis of experimental data and determination of parameters

Elastic moduli were determined in a standard manner from the slope of the loading curves. To determine the model parameters based on the data from the completed experiments, we used the procedure outlined in (Stefanov et al., 2011). The points of elasticity limit (2) and ultimate strength (3) were determined on the curve of stress versus axial strain (Fig. 3) for each experiment. Point (1) on the graph corresponds to the values when the nonlinearity of the initial loading stage becomes insignificant (Grueschow and Rudnicki, 2005; Stefanov, 2018).

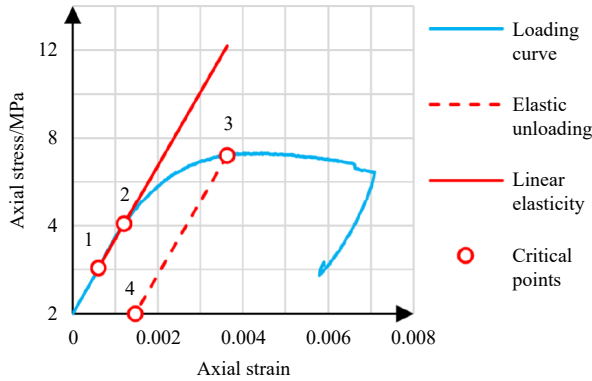


图3 室内试验中获得的应力与应变关系示例

Fig. 3 An example of the dependence of stress on strain obtained during a laboratory experiment

For each experiment, the dependence of the intensity of tangential stresses  $I_2$ :

$$I_2 = (\sigma_a - \sigma_r) / \sqrt{3} \quad (7)$$

on pressure  $I_1$ :

$$I_1 = (\sigma_a + 2\sigma_r) / 3 \quad (8)$$

was analyzed to define yield surface parameters.

As noted above, compaction is observed for loading at high values of confining stress. Therefore, only a fraction of the experiments is used to determine the parameters of the linear plasticity criterion (2) using the least squares method. All experiments, apart from the last pair (which are characterized by clear compaction – Fig.

2), were studied with respect to the elasticity limit. Elasticity limit was chosen based on the maximum volumetric strain during the loading which is in line with common approaches (Bieniawski, 1967). Given the possible errors discussed earlier, the error for the definition of stress state parameters for the elasticity limit was defined as follows. All stress states with volumetric strain exceeding 95% of their maximum value were considered to be within the error bar for the elasticity limit. Equations (7) and (8) were therefore used to plot the relationship between the first and second invariants of the stress tensor at the elasticity limit (Fig. 4).

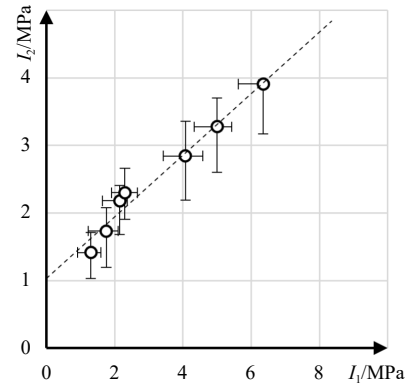


图4 Drucker-Prager 屈服面参数的测定

Fig. 4 Determination of Drucker-Prager yield surface parameters

It is worth noting that error bars are not symmetric for one dot corresponding to experiment 7, where the sample demonstrated a failure soon after the elasticity limit (Fig. 2). A linear approximation was constructed (dotted line) using the least squares method: the use of the linear yield surface defined by Equation 2 proves to be valid based on the plotted error bars. The resultant yield surface parameters are: internal friction angle coefficient  $\alpha = 0.46$ , initial cohesion  $Y_0 = 1.03$  MPa.

In turn, the critical points obtained during experiments 8 and 9 should determine the parameters  $a$ ,  $b$  and  $\sigma_0$  from expression (5). Due to the small amount of experimental data, a matching condition is additionally used: the yield function must be continuously differentiable; therefore, at the matching point with coordinates  $(I_1^*, I_2^*)$ , the following equations must be satisfied:

$$a^2 = \frac{(I_2 - \sigma_0)^2 b^2}{b^2 - (\alpha I_1 + Y)^2}, \quad (9)$$

$$b = \alpha a \left( \frac{a^2 - (I_2 - \sigma_0)^2}{(I_2 - \sigma_0)^2} \right)^{1/2}. \quad (10)$$

These equations meet the requirements of continuity of the yield function  $f$  and its differential. Equations (9) and (10) establish unambiguous correspondences between the parameters of functions (2) and (5).

While parameters  $\alpha$  and  $Y$  are determined according to the data of experiments 1 – 6,  $\sigma_0$  requires the use of the data of experiments 8 and 9. The values ( $I_1^*$ ,  $I_2^*$ ) were taken equal to the critical values obtained for experiment 7, in which the volumetric deformation returned to zero.

Note that there is a certain data spread, which may be associated with the ambiguity in determining the elasticity limit.

Neglecting the change in the internal friction angle during the deformation of the samples, during the transition from the elastic to the plastic state, and also taking into account that the final yield surface was determined more accurately, the initial yield surface was drawn parallel to it.

From the constructed yield surfaces, the following were determined: internal friction coefficient  $\alpha = 0.51$ , initial cohesion  $Y_0 = 0.95$  MPa, final cohesion  $Y^* = 2.22$ , hardening coefficient, respectively, equal to 1.34; as well as model parameters (5) in the compaction region: for the initial state  $a = 1.84$  MPa,  $b = 2.50$  MPa,  $\sigma_0 = 3.32$  MPa; for the final state  $a = 2.88$  MPa,  $b = 4.33$  MPa,  $\sigma_0 = 4.62$  MPa.

The dependence of the increments of the first invariant of the plastic deformation tensor  $\Delta I = (\epsilon_a + 2\epsilon_r)/3$  on the intensity of shear plastic deformations  $\gamma = 2(\epsilon_a - \epsilon_r)/\sqrt{3}$  was plotted (Fig. 5) to determine the dilatancy coefficient. To calculate the average value of the dilatancy coefficient, the increments were determined as the difference in the values of plastic deformations at points 2 and 3 (Fig. 3). The value of the dilatancy coefficient averaged over a series of experiments was taken equal to 0.09.

#### 4 Determination of uniaxial tensile strength

One of the key characteristics of the model material

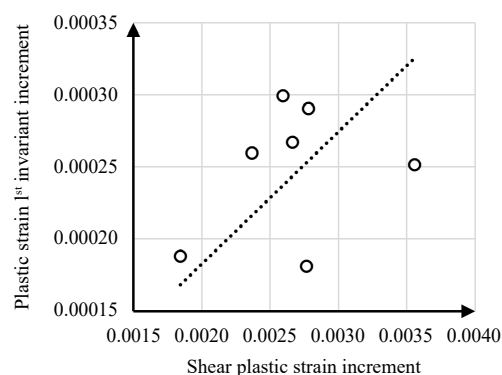


图5 试验过程中塑性变形张量第一不变量的增量与剪切塑性变形强度增量的关系

Fig. 5 Dependence of the increment of the first invariant of the plastic deformation tensor on the increment of the intensity of shear plastic deformations for a series of experiments

that determines the process of occurrence and development of hydraulic fractures is uniaxial tensile strength. While the aforementioned mathematical model was successfully utilized to describe the sample behavior in compressive stress state, tensile strength is also an important parameter for constitutive modeling. Therefore, an additional series of laboratory tests was carried out to determine the uniaxial tensile strength using the “Brazilian” method. A view of the laboratory setup is shown in the figure (Fig. 6).

In this series of experiments, described in detail in

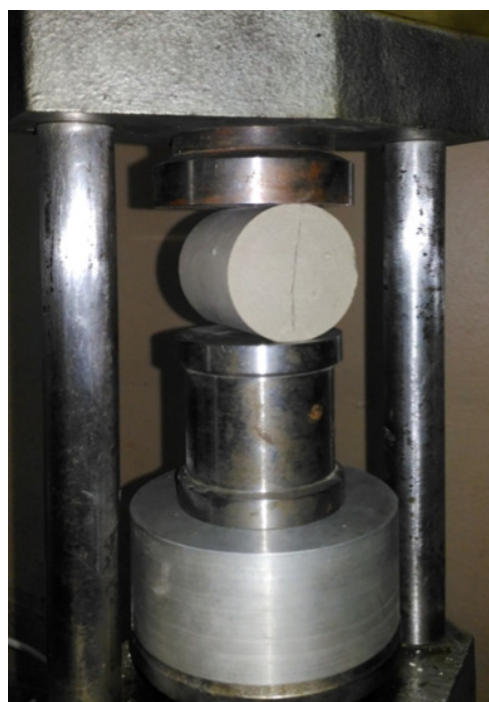


图6 “巴西劈裂法”测试后破裂试样

Fig. 6 Destroyed sample after testing using the “Brazilian” method

(Novikova et al., 2023), samples from a model material were used. The diameter and length of the samples were 40 mm and 42 mm, respectively. During testing using a hand press, the sample was placed between parallel steel plates. The uniaxial tensile strength UTS for such experiments was calculated using the formula  $\sigma_p = KP/S$ , where  $K = 2/\pi$  when loaded with plates,  $P$  is the breaking force, and  $S$  is the product of the length of the sample and its diameter. The test results using the “Brazilian” method are shown in Table 2.

表 2 “巴西劈裂法”测试结果

Table 2 Results of the “Brazilian” test

Sample number	Breaking force $P$ /kN	Uniaxial tensile strength UTS/MPa
1	1.7	0.6
2	2.6	1.0
3	2.0	0.8
4	2.1	0.8
5	1.8	0.7
6	2.3	0.9

From the measurements taken, the average tensile strength was determined as 0.8 MPa. Note that this value turned out to be very close to the values of the cohesion coefficient.

## 5 Validation of the model based on three-dimensional numerical simulation

The next stage in constructing a material behavior model is the clarification of its parameters. It is necessary not only to check the adequacy of the model to describe the deformation process, but it is also required to clarify the parameters due to the ambiguity of their definition and the spread of the experimental data. Note that this task is not trivial; as a result of modeling, it is necessary to reproduce the behavior of samples in a series of experiments, taking into account changes in their properties during deformation and dependence on compressive conditions. For each experiment, it is necessary to obtain a correspondence between two curves: the dependence of the axial load on the axial and radial (or volumetric) strain.

Numerical modeling of the behavior of rock samples was carried out under the conditions corresponding to the experimental data. A 3D numerical modeling program (Stefanov and Bakeev, 2015) based on the finite-difference method for solving a system of equations for the dynamics of an elastoplastic medium (Wilkins, 1999) was used. The loading was carried out very slowly and smoothly so that the dynamic effects did not have a noticeable influence on the solution. The application of the explicit scheme turns out to be very efficient in terms of computational resources and is also easy to implement using the parallelization algorithms that are required to solve 3D problems. The main details related to the approach used in 2D and 3D formulations are given in (Stefanov et al., 2011; Stefanov and Bakeev, 2015).

Initial and boundary conditions were chosen to reproduce experimental setup conditions: a sample, modeled as a deformable cylindrical body was subjected to constant radial stress and gradually increasing axial stress. At the initial loading stage, a uniform pressure distribution equal to radial stress was stated as an initial condition. After that, while keeping the load on the lateral faces constant, the axial displacement of the top and bottom faces was gradually changed to simulate the kinematic compression of the core specimens. Axial and radial displacements, as well as averaged stresses on the end faces of the specimen, were recorded as output parameters, similar to the recording of measurements during the experiments. Localization of plastic strains could be the only reason for instability in the numerical scheme. However, the current formulation of the problem does not allow for localization, which would enable us to address numerical instability specifically.

Calculations carried out using parameters that were determined from experimental data (Table 3; Calculation 1) have shown a rather noticeable discrepancy between the obtained loading diagrams and the experimental results (Fig. 7; Calculation 1). This discrepancy is due to averaging the parameters over a series of experiments, as well as a certain ambiguity in their determination. Moreover, the discrepancy between different experiments corresponding to different lateral compression pressure differs significantly and increases with this pressure. This

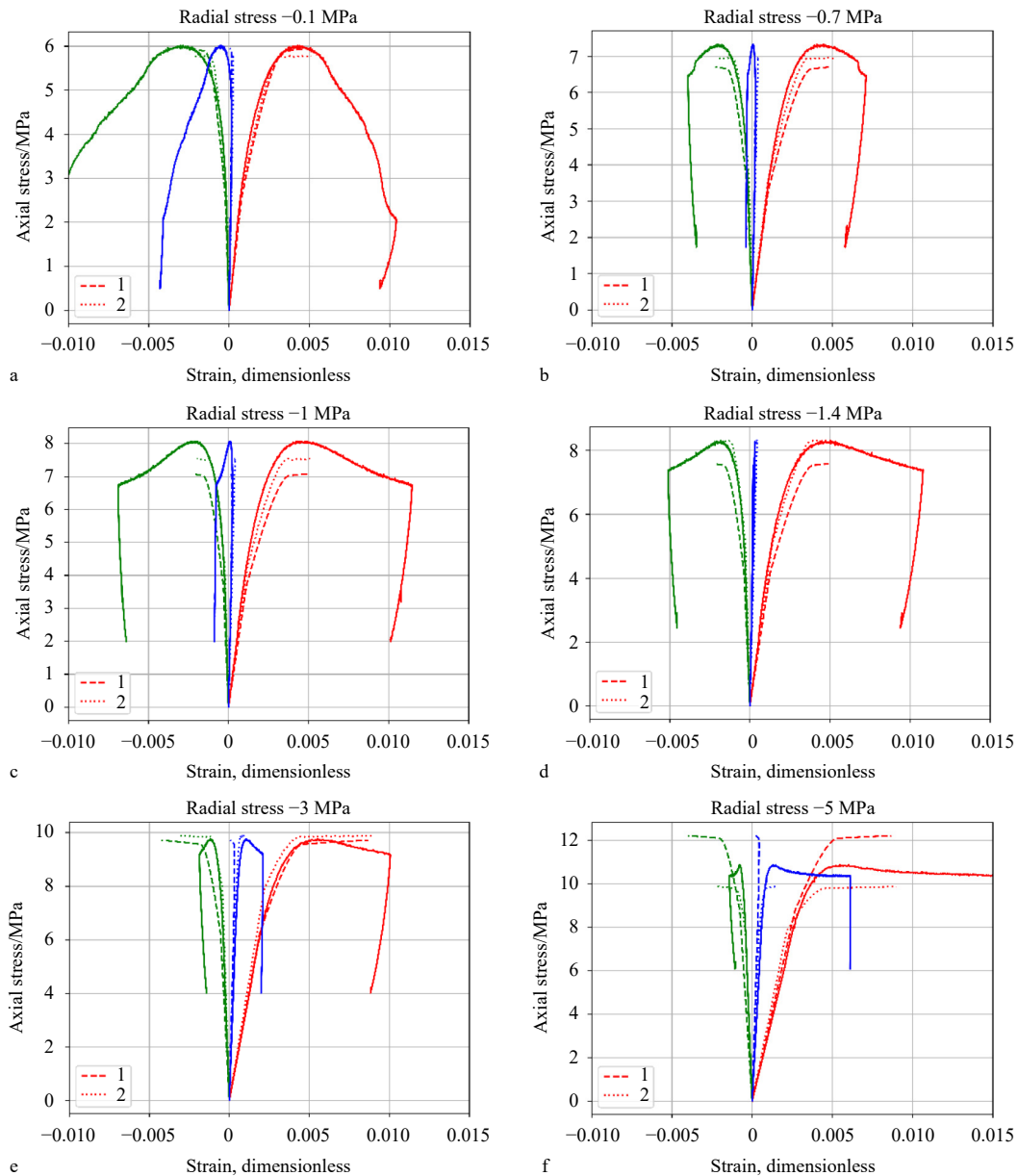
indicates an underestimated value of the internal friction coefficient and, as a result, errors in calculating the initial cohesion and hardening coefficients. Therefore, a series of

calculations was necessary with refinement of the parameters (Table 3; Calculation 2) until satisfactory compliance was achieved (Fig. 7; Calculation 2).

表 3 特定材料特性

Table 3 Specific material properties

Calculation number	Density/(g/cm <sup>3</sup> )	Shear modulus/MPa	Compression modulus/MPa	Initial cohesion/MPa	Hardening coefficient	Dilation coefficient	Critical strain	Internal friction coefficient	$\sigma_0$ , MPa	$\epsilon^*$
1	1.66	1276	2586	1.028	1.34	0.09	0.0029	0.46		
2	1.66	1517	1980	0.775	1.48	0.09	0.0028	0.68	5.5	0.5



实线—试验数据；虚线—1号数据的计算结果；点虚线—2号数据的计算结果

图 7 不同围压条件下轴向应力与轴向应变（红线）、径向应变（绿线）和体积应变（蓝线）的关系

Fig. 7 Axial stress dependence on axial strain (red line), radial strain (green line), and volumetric strain (blue line) with different radial stresses.

solid lines—experimental data; dashed lines—calculation with data No. 1; dotted lines—calculation with data No. 2

As a result, it was possible to find the necessary values of the model parameters that make it possible to describe all features of the behavior of the considered rock samples in the entire range of loading conditions with satisfactory accuracy. Within the framework of the model, a series of experiments with different lateral compression pressures were properly reproduced.

The primary requirement for numerical modeling results was the proper reproduction of the experimental data for the major part of the loading process. Moreover, all components of strain had to be in quantitative agreement with experiments: it is not enough to reconstruct only the ‘axial stress vs. axial strain’ curve, which could have been done without the need to introduce a non-associated plastic flow law. Axial stress dependency on volumetric strain appears to be a crucial factor in evaluating the capability of the theoretical model to reproduce test results.

The comparison can be seen in Fig. 6, where the dotted and dashed lines (numerical modeling results) overlap with experimentally obtained curves for the major part of the loading. Relative error in the elastic zone generally does not exceed 5% for the volumetric strain. After the inelastic strains start to accumulate, the discrepancy increases. Depending on the simulation parameters (scenario 1 or 2 from Table 3), the error may become significant, proving the need to adjust model parameters – turn from calculation scenario 1 to scenario 2. Lower levels of residual stress correspond to a smaller discrepancy between numerical modeling and

experimental data: non-adjusted model parameters prove to be incapable of reproducing compaction under the given condition; yield stress level tends to be underestimated for the unadjusted model. The major disagreement between obtained results starts after peak stress: as plastic flow law is used for numerical modeling, the rupture process, which takes place after failure, cannot be totally adequately described. Softening of the sample and the following unloading require a separate modeling procedure with the proper parameters introduced. Within the scope of the current study, we abstain from considering the post-rupture process, limiting the model solely to the pre-failure process. The adjusted model provided numerical results with the highest discrepancy at a level of approximately 10% for residual stress of 3 MPa, which is within the acceptable range for typical reservoir geomechanics problems, where the primary uncertainty factor is an estimation of in-situ stresses from geophysical data.

The deformation of the specimens was modeled on the adapted computational mesh shown in Fig. 8. For the numerical method used, such a grid is suitable and also very simple to generate. The calculations were performed on a grid containing  $96 \times 50 \times 50$  non-structured wedge cells. This number is sufficient to describe the deformation of the specimens at all stages of deformation. This was confirmed by many previously performed calculations of the deformation process (Stefanov and Zharasbaeva, 2022; Stefanov, 2023). In this work, only the stable stage of deformation was considered, so that the process proceeds with hardening. At this stage, the behavior of the

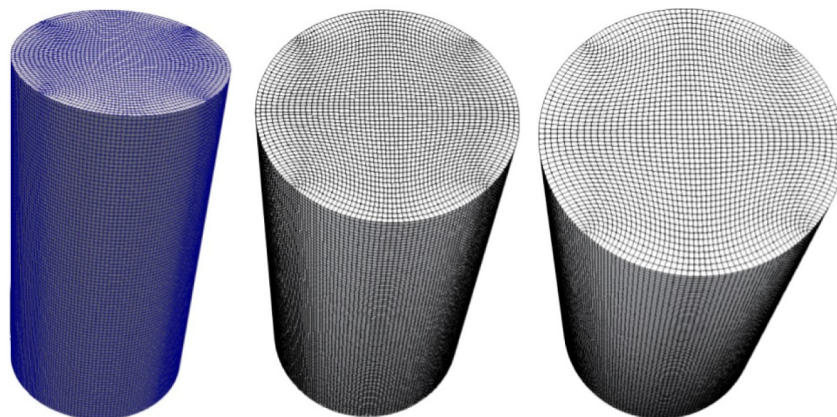


图 8 数值模型网格划分

Fig. 8 Modeling mesh

specimen can be modeled on a less detailed mesh. The established modeling procedure was not changed, and therefore, the calculations were performed with excessive accuracy.

Two elastic moduli, compression modulus  $K$ , and shear modulus  $\mu$ , along with ten plasticity parameters, are used to model the process within the elastic-plastic model outlined. Plasticity parameters include: initial cohesion  $Y$ ; hardening coefficient  $h$ ; dilatancy coefficient  $\beta$ ; critical strain  $\gamma^*$ ; internal friction coefficient  $\alpha$ ; parameters of Cap  $\sigma_0$ ,  $\sigma_1$ ; parameter of Cap expansion  $m$ ; porosity  $\varepsilon^*$ ; parameter of dilatancy–pressure relation  $n$ .

When compaction was added to the model, the calculated curves of the dependence of axial stress on volumetric strain for new experiments (8, 9) turned to the right, whereas the direction for the first experiments did not change (Fig. 7).

The model based on the combined Drucker-Prager/Cap model was used to simulate the deformation processes of the samples. This model allows describing the deformation processes of rocks of various porosities, taking into account dilatancy and compaction. It has been successfully used to simulate the behavior of rock samples in order to develop variants of parameter dependencies, as well as calibration for describing deformation processes in the rocks for 2D and 3D problems. Obviously, in each specific case, it may be necessary to apply additional dependencies that describe the changes of model parameters during deformation, for example, hardening, internal friction, and dilatancy parameters. It is for this purpose that the model is calibrated using experimental data. We do not claim that the model is universal, but with its help we managed to describe many deformation processes for rocks of different types and under different conditions: core tests (Stefanov et al., 2011; Stefanov and Zharasbaeva, 2022), well surrounding rock masses (Garavand et al., 2020), tectonic processes in the upper layers of the Earth's crust (Stefanov and Bakeev, 2015), and others.

The obtained results make it possible to claim that the suggested method is capable of modeling the inelastic behavior of the studied samples. Nevertheless, there are still certain limitations on both the model and the obtained

parameters. Firstly, it is clear that the obtained model parameters listed in the tables and discussed in these sections can only be used for the particular material in use. Application of the same model to other materials requires a series of triaxial loading experiments with a wide range of radial stress levels. The two-step calibration procedure described here should be conducted in a similar way. Moreover, careful analysis of experimental errors should be conducted to conclude whether the model itself is capable of describing the material behavior. For example, if the  $I_2$  vs  $I_1$  plot (Fig. 4) of elasticity limits suggests a nonlinear relationship, the Drucker-Prager yield surface may be incapable to adequately describe the inelastic deformation of the material, and external complication of the yield surface is required. The final limitation is clearly the neglect of the intermediate principal stress effect on inelastic behavior. A number of recent studies consider this effect using true triaxial loading tests, as described in comprehensive reviews (Mahetaji and Brahma, 2024). On the one hand, such tests provide valuable information on the mechanical behavior of rock samples subjected to considerably varying stresses. On the other hand, both the conduction of such tests and the analysis of experimental results imply a number of problems that are not yet completely solved. If the intermediate principal stress effect on the inelastic deformation of a rock mass can be neglected, and the mathematical equations are capable of reproducing critical points of loading – elasticity limit and peak stress – then the suggested model can properly predict quasi-static deformation.

To further analyze the mechanical behavior of an elastic-plastic medium, the parameters from calculation 2 were used, which were as close to the experimental data as possible and took the process of material compaction into account. An additional value for the uniaxial tensile strength of the material is required to apply the model to solve practical rock mechanics problems. A description of the definition of these material properties is given below.

## 6 Conclusions

An analysis of the test results for triaxial compression of samples of a model environment was

carried out. The experimental stress-strain curves were compared with the calculated curves obtained for a plasticity model with a non-associated flow law taking the hardening of the medium into account. The main conclusions are as followings:

(1) It was found that for the entire range of applied lateral loads, the elastic limit varied from 2 to 4 MPa, after which the material began to behave plastically.

(2) It was also determined that at lateral loads  $\geq 3$  MPa, compaction began to appear in the material beyond the yield point.

(3) Judging by the dependence of volumetric strains under a lateral load equal to 1.4 MPa, compaction should begin to appear even at lower lateral loads than 3 MPa.

(4) In addition, the uniaxial tensile strength of the material is also necessary for modeling the process of hydraulic fracturing, so this parameter was determined as well.

(5) Taking the plastic behavior of the material into account is necessary when moving on to modeling the hydraulic fracturing process in such a material, and the resultant plasticity parameters for the model material can be used for numerical modeling of elastoplastic deformation of the rock under consideration, including the processes of hydraulic fracture growth in a poroelastoplastic medium.

## References

- AMOUR F, HAJIABADI M R, NICK H M, 2023. Impact of uncertainties associated with the choice of the yield stress on the prediction of subsurface reservoir compaction: a field study[J]. *International Journal of Rock Mechanics and Mining Sciences*, 161: 105280.
- BÉSUELLE P, DESRUES J, RAYNAUD S, 2000. Experimental characterisation of the localisation phenomenon inside a Vosges sandstone in a triaxial cell[J]. *International Journal of Rock Mechanics and Mining Sciences*, 37(8): 1223-1237.
- BIENIAWSKI Z T, 1967. Mechanism of brittle fracture of rock: part I—theory of the fracture process[J]. *International Journal of Rock Mechanics and Mining Sciences & Geomechanics Abstracts*, 4(4): 395-406.
- CASSIANI G, BROVELLI A, HUECKEL T, 2017. A strain-rate-dependent modified Cam-Clay model for the simulation of soil/rock compaction[J]. *Geomechanics for Energy and the Environment*, 11: 42-51.
- CHEN Z L, SHI H Z, XIONG C, et al., 2023. Effects of mineralogical composition on uniaxial compressive strengths of sedimentary rocks[J]. *Petroleum Science*, 20(5): 3062-3073.
- DE PATER C J, CLEARY M P, QUINN T S, et al., 1994. Experimental verification of dimensional analysis for hydraulic fracturing[J]. *SPE Production & Facilities*, 9(4): 230-238.
- DRUCKER D C, PRAGER W, 1952. Soil mechanics and plastic analysis or limit design[J]. *Quarterly of Applied Mathematics*, 10(2): 157-165.
- ESCRIBANO D E, NASH D F T, DIAMBRA A, 2019. Local and global volumetric strain comparison in sand specimens subjected to drained cyclic and monotonic triaxial compression loading[J]. *Geotechnical Testing Journal*, 42(4): 1006-1030.
- FU J W, LABUZ J F, GUO M D, et al., 2022. Experimental and numerical investigations on hydraulic fracture growth using rock-like resin material containing an injecting inner pre-crack[J]. *Journal of Petroleum Science and Engineering*, 213: 110424.
- GARAGASH D I, 2019. Cohesive-zone effects in hydraulic fracture propagation[J]. *Journal of the Mechanics and Physics of Solids*, 133: 103727.
- GARAGASH I A, DUBINYA N V, RUSINA O A, et al., 2018. Estimation of rock strength properties from triaxial test data[J]. *Geophysical Research*, 19(3): 57-72.
- GARAVAND A, STEFANOV Y P, REBETSKY Y L, et al., 2020. Numerical modeling of plastic deformation and failure around a wellbore in compaction and dilation modes[J]. *International Journal for Numerical and Analytical Methods in Geomechanics*, 44(6): 823-850.
- GRUESCHOW E, RUDNICKI J W, 2005. Elliptic yield cap constitutive modeling for high porosity sandstone[J]. *International Journal of Solids and Structures*, 42(16-17): 4574-4587.
- HAJIABADI M R, NICK H M, 2020. A modified strain rate dependent constitutive model for chalk and porous rock[J]. *International Journal of Rock Mechanics and Mining Sciences*, 134: 104406.
- HE W H, CHEN K Y, HAYATDAVOUDI A, et al., 2019. Effects of clay content, cement and mineral composition characteristics on sandstone rock strength and deformability behaviors[J]. *Journal of Petroleum Science and Engineering*, 176: 962-969.
- JIAO Y, ZUO Y J, WEN Z J, et al., 2024. Crack-tip propagation laws and energy evolution of fractured sandstone[J]. *Engineering Failure Analysis*, 166: 108832.
- JIN Y J, MENG L D, LYU D Y, et al., 2023. Risk assessment of fault reactivation considering the heterogeneity of friction strength in the BZ34-2 oilfield, Huanghekou Sag, Bohai Bay basin, China[J]. *Petroleum Science*, 20(5): 2695-2708.
- LIU S L, LI P F, HU K, et al., 2023. Constitutive modeling of brittle-ductile transition in porous rocks: formulation, identification and simulation[J]. *Acta Mechanica*, 234(5): 2103-2121.
- LYAKHOVSKY V, PANTELEEV I, SHALEV E, et al., 2022. A new anisotropic poroelasticity model to describe damage accumulation during cyclic triaxial loading of rock[J]. *Geophysical Journal International*, 230(1): 179-201.
- MA S, LI G M, ZHANG Y J, et al., 2024. Propagation behavior of coal crack induced by liquid CO<sub>2</sub> phase change blasting considering blasting pressure effects[J]. *PLoS One*, 19(1): e0313360.
- MAHETAJI M, BRAHMA J, 2024. A critical review of rock failure criteria: a scope of machine learning approach[J]. *Engineering Failure Analysis*, 159: 107998.

- NIKOLAEVSKII V N, 1971. Governing equations of plastic deformation of a granular medium: PMM vol. 35, n<sup>o</sup>6, 1971, pp. 1070–1082[J]. *Journal of Applied Mathematics and Mechanics*, 35(6): 1017-1029.
- NOVIKOVA E V, TRIMONOVA M A, DUBINYA N V, et al., 2023. Estimation of breakdown pressure in laboratory experiments on hydraulic fracturing[J]. *Materials Physics and Mechanics*, 51(5): 52-65.
- OMAR T, SADREKARIMI A, 2015. Effect of triaxial specimen size on engineering design and analysis[J]. *International Journal of Geo-Engineering*, 6(1): 5.
- OMLIN S, RÄSS L, PODLADCHIKOV Y Y, 2018. Simulation of three-dimensional viscoelastic deformation coupled to porous fluid flow[J]. *Tectonophysics*, 746: 695-701.
- RONG G, LIU G, HOU D, et al., 2013. Effect of particle shape on mechanical behaviors of rocks: a numerical study using clumped particle model[J]. *The Scientific World Journal*, 2013: 589215.
- SATHAR S, REEVES H J, CUSS R J, et al., 2012. The role of stress history on the flow of fluids through fractures[J]. *Mineralogical Magazine*, 76(8): 3165-3177.
- SCHWAB D R, BIDGOLI T S, TAYLOR M H, 2017. Characterizing the potential for injection-induced fault reactivation through subsurface structural mapping and stress field analysis, Wellington Field, Sumner County, Kansas[J]. *Journal of Geophysical Research: Solid Earth*, 122(12): 10132-10154.
- STEFANOV Y P, CHERTOV M A, AIDAGULOV G R, et al., 2011. Dynamics of inelastic deformation of porous rocks and formation of localized compaction zones studied by numerical modeling[J]. *Journal of the Mechanics and Physics of Solids*, 59(11): 2323-2340.
- STEFANOV Y P, BAKEEV R A, 2015. Formation of flower structures in a geological layer at a strike-slip displacement in the basement[J]. *Izvestiya, Physics of the Solid Earth*, 51(4): 535-547.
- STEFANOV Y P, 2018. Some nonlinear rock behavior effects[J]. *Physical Mesomechanics*, 21(3): 234-241.
- STEFANOV Y P, ZHARASBAEVA D K, 2022. Loading diagrams and parameters of the model of elastic-pseudoplastic deformation of black shale rocks of the Bazhenov formation[J]. *Russian Journal of Geophysical Technologies*(3): 13-24. (in Russian)
- STEFANOV Y P, 2023. Constitutive model of rock, nonlinearity and localization[J]. *Reviews on Advanced Materials and Technologies*, 5(3): 30-38.
- SUN C, BORGOMANO J V M, FORTIN J, et al., 2020. Effect of pore collapse and grain crushing on the frequency dependence of elastic wave velocities in a porous sandstone[J]. *Rock Mechanics and Rock Engineering*, 53(11): 5081-5093.
- SUN W J, WANG L B, WANG Y Q, 2017. Mechanical properties of rock materials with related to mineralogical characteristics and grain size through experimental investigation: a comprehensive review[J]. *Frontiers of Structural and Civil Engineering*, 11(3): 322-328.
- TAN X, KONIETZKY H, FRÜHWIRT T, 2015. Numerical simulation of triaxial compression test for brittle rock sample using a modified constitutive law considering degradation and dilation behavior[J]. *Journal of Central South University*, 22(8): 3097-3107.
- TANG Y L, LI J C, WANG D P, et al., 2024. An energy-driven crushing-plasticity coupling model for grain crushing in porous rocks[J]. *International Journal of Rock Mechanics and Mining Sciences*, 183: 105931.
- TRIMONOVA M, BARYSHNIKOV N, ZENCHENKO E, et al., 2017. The study of the unstable fracture propagation in the injection well: numerical and laboratory modeling[C]//Proceedings of SPE Russian Petroleum Technology Conference. Moscow: SPE: 187822-MS.
- VAN DAM D B, PAPANASTASIOU P, DE PATER C J, 2002. Impact of rock plasticity on hydraulic fracture propagation and closure[J]. *SPE Production & Facilities*, 17(3): 149-159.
- VERMEER P A, DE BORST R, 1984. Non-associated plasticity for soils, concrete and rock[J]. *Heron*, 29(3): 1-64.
- VESELOVSKIY R V, DUBINYA N V, PONOMAREV A V, et al., 2022. Shared research facilities "petrophysics, geomechanics and paleomagnetism" of the Schmidt institute of physics of the earth RAS[J]. *Geodynamics & Tectonophysics*, 13(2): 0579.
- WANG D P, LI J C, ZOU C J, et al., 2024. The influence of morphology and the loading-unloading process on discontinuity stress states observed via photoelastic technique and its inspiration to induced seismicity[J]. *International Journal of Rock Mechanics and Mining Sciences*, 182: 105893.
- WANG J, XIE H P, MATTHAI S K, et al., 2023. The role of natural fracture activation in hydraulic fracturing for deep unconventional geo-energy reservoir stimulation[J]. *Petroleum Science*, 20(4): 2141-2164.
- WENG X W, KRESSE O, CHUPRAKOV D, et al., 2014. Applying complex fracture model and integrated workflow in unconventional reservoirs[J]. *Journal of Petroleum Science and Engineering*, 124: 468-483.
- WILKINS M L, 1999. Computer simulation of dynamic phenomena[M]. Berlin: Springer: 1-260.
- WILLIAMS B, HEARD W, GRAHAM S, et al., 2020. Effect of specimen geometry on triaxial compressive response of high-strength concrete[J]. *Construction and Building Materials*, 244: 118348.
- WONG T F, BAUD P, 2012. The brittle-ductile transition in porous rock: a review[J]. *Journal of Structural Geology*, 44: 25-53.
- YANG P J, MIAO S J, CAI M F, et al., 2024. Real-time porosity inversion of rock based on the ultrasonic velocity and its compression-damage coupled model under triaxial compression[J]. *Scientific Reports*, 14(1): 29252
- YANG S Q, JING H W, WANG S Y, 2012. Experimental investigation on the strength, deformability, failure behavior and acoustic emission locations of red sandstone under triaxial compression[J]. *Rock Mechanics and Rock Engineering*, 45(4): 583-606.
- YARUSHINA V M, PODLADCHIKOV Y Y, WANG L H, 2020. Model for (de)compaction and porosity waves in porous rocks under shear stresses[J]. *Journal of Geophysical Research: Solid Earth*, 125(8): e2020JB019683.
- YIMSIRI S, SOGA K, 2002. A review of local strain measurement systems for triaxial testing of soils[J]. *Journal of the Southeast Asian Geotechnical Society*, 33(1): 41-52.
- ZHANG B C, LIANG Y N, ZOU Q L, et al., 2024. Damage and hardening evolution characteristics of sandstone under multilevel creep-fatigue loading[J]. *Geomechanics and Geophysics for Geo-Energy and Geo-Resources*, 10(1): 43.